Letter

Mooij Law Violation from Nanoscale Disorder

Aifeng Wang,* Lijun Wu, Qianheng Du, Muntaser Naamneh, Walber Hugo Brito,
AM Milinda Abeykoon, Wojciech Radoslaw Pudelko, Jasmin Jandke, Yu Liu, Nicholas C. Plumb,
Gabriel Kotliar, Vladimir Dobrosavljevic, Milan Radovic, Yimei Zhu, and Cedomir Petrovic*

Read Online

ACCESS | Metrics & More | Article Recommendations | Supporting Information

ABSTRACT: Nanoscale inhomogeneity can profoundly impact properties of two-dimensional van der Waals materials. Here, we reveal how sulfur substitution on the selenium atomic sites in $Fe_{1−y}Se_{1−x}S_x$ ($0 \leq x \leq 1$, $y \leq 0.1$) causes Fe−Ch (Ch = Se, S) bond length differences and strong disorder for $0.4 \leq x \leq 0.8$. There, the superconducting transition temperature T_c is suppressed and disorder-related scattering is enhanced. The high-temperature metallic resistivity in the presence of strong disorder exceeds the Mott limit and provides an example of the violation of Matthiessen's rule and the Mooij law, a dominant effect when adding moderate disorder past the Drude/Matthiessen's regime in all materials. The scattering mechanism responsible for the resistivity above the Mott limit is unrelated to phonons and arises for strong Se/S atom disorder in the tetrahedral surrounding of Fe. Our findings shed light on the intricate connection between the nanostructural details and the unconventional scattering mechanism, which is possibly related to charge-nematic or magnetic spin fluctuations.

KEYWORDS: disorder, defects, electrical transport, superconductivity
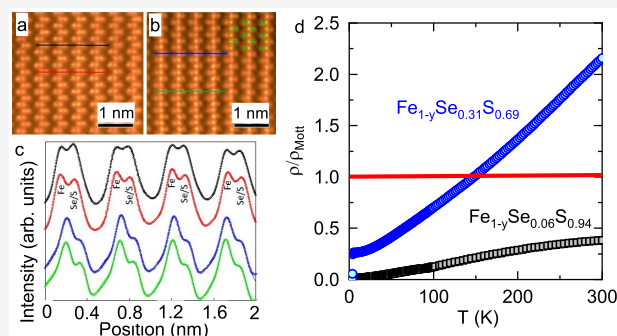
Atomic defects are ubiquitous in two-dimensional (2D) materials with van der Waals bonds and have the potential to significantly modulate properties and bring about useful functionalities.[1,2] Together with interactions due to charge, orbital, spin, and lattice degrees of freedom, inhomogeneity due to nanoscale defects leaves a significant imprint on electronic and thermal transport properties.[3,4]

The Boltzmann equation has been widely used in the past century to explain transport properties in solids.[5−9] A cornerstone of the Boltzmann transport model is Matthiessen's rule, which treats all scattering processes as independent and additive. The rule is a common method in treating scattering, though discrepancies have been observed in several strongly correlated materials.[10−12] In metals, it leads to a positive resistivity slope $d\rho/dT > 0$ since thermally induced scattering increases electrical resistivity. The rule also predicts that as disorder increases so does the elastic scattering ρ_0, whereas the temperature-dependent inelastic contribution is unaffected. This is indeed seen in many weakly disordered metals where resistivity $\rho_0 = \rho \rightarrow 0$ approaches Mott−Ioffe−Regel limit, where scattering lengths become very short and correspond to interatomic distances, leading to Anderson localization.[13−15] At strong disorder, Mooij noticed a general trend: as the metallic resistivity slope changes and eventually changes sign, the resistivity slope is inversely proportional to ρ_0. This has been observed even at very high temperatures above the Debye temperature.[16,17]

Here, we report a strong violaton of the Matthiessen's rule and Mooij law arising from nanoscale inhomogeneity of disordered Fe atomic vacancy defects and Fe−Ch (Ch = Se, S) bond distances in $Fe_{1−y}Se_{1−x}S_x$ ($0 \leq x \leq 1$, $y \leq 0.1$), created by chemical substitution on chalcogen atomic sites in FeSe and FeS superconductors.[18,19] FeSe also features a nematic state below T_s = 91 K driven by charge-orbital or spin degrees of freedom, instead of the weak tetragonal-to-orthorhombic distortion of the lattice.[20−23] We observe a vast region for $0.4 \leq x \leq 0.8$ where the effects of disorder on electronic transport is strong, as seen in the dimensionless quantity $k_F l <$ 1, where k_F is the Fermi wavenumber and $l = v\tau$ is the mean free path of electron wave pocket with group velocity v and elastic scattering time τ between two successive scattering events. There, in contrast to FeSe or FeS, Fe atomic vacancies and Fe−Ch bond lengths exhibit spatial inhomogeneity on the nanoscale. In this x range, resistivity is metallic at high temperature, even though $k_F l \sim 1$ is widely accepted to coincide with the Mott−Ioffe−Regel criterion associated with
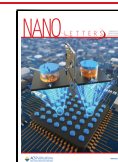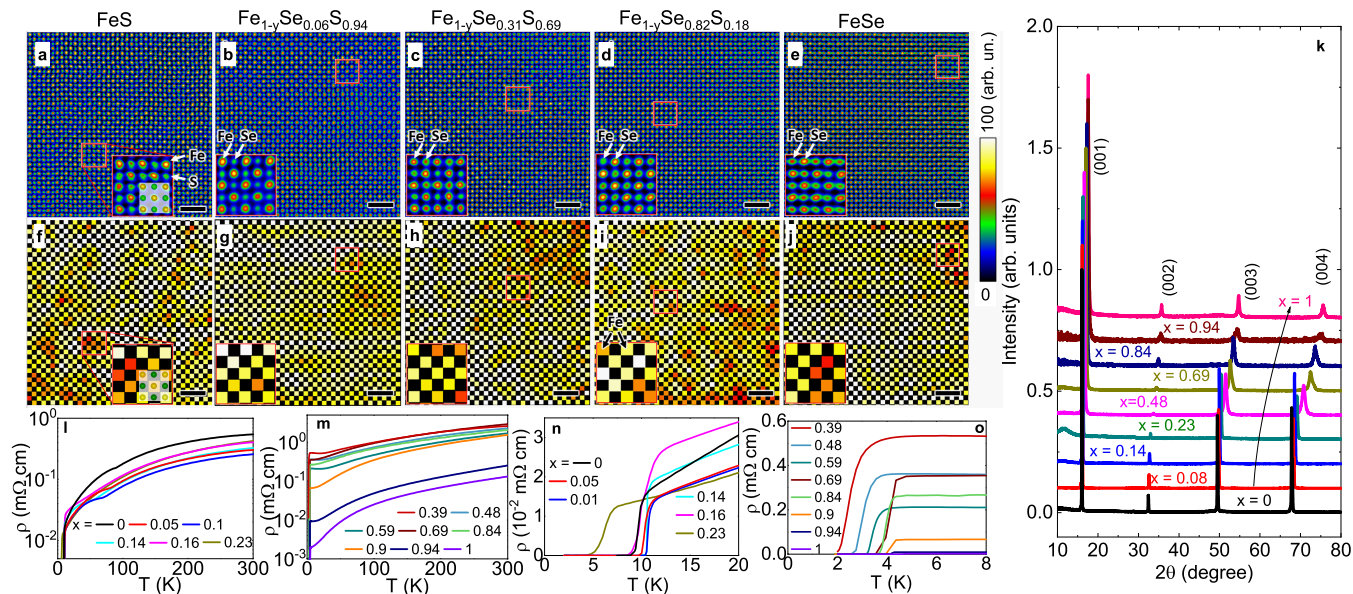
Figure 1. (a-e) STEM-HAADF images with the incident beam along the [001] direction for (a) FeS, (b) $Fe_{1-y}Se_{0.06}S_{0.94}$, (c) $Fe_{1-y}Se_{0.31}S_{0.69}$, (d) $Fe_{1-y}Se_{0.82}S_{0.18}$, and (e) FeSe single crystals. Scale bar 1 nm. Note that the contrast of Fe columns is stronger than that of S/Se columns in FeS, $Fe_{1-y}Se_{0.06}S_{0.94}$, and $Fe_{1-y}Se_{0.31}S_{0.69}$ but becomes weaker in $Fe_{1-y}Se_{0.82}S_{0.18}$ and FeSe. The image contrast in (d,e) is reduced to avoid displaying saturated Se/S columns. (f–j) Peak intensity map of Fe columns refined from the corresponding images in the first row. Each square represents a Fe column. Scale bar 1 nm. The insets are the magnified images from the area marked by the red squares. The [001] projection of FeS is shown in the insets in (a,f), with yellow and green spheres representing Fe and S atoms, respectively. The map clearly shows the peak intensity variation of Fe columns, indicating that the Fe vacancies vary from column to column. (k) Single crystal XRD patterns at room temperature. Patterns are offset for clarity. (l–o) Resistivity of $Fe_{1-y}Se_{1-x}S_x$. (n) shows an enlarged low-temperature region for (l); (o) shows an enlarged low-temperature region for (m).
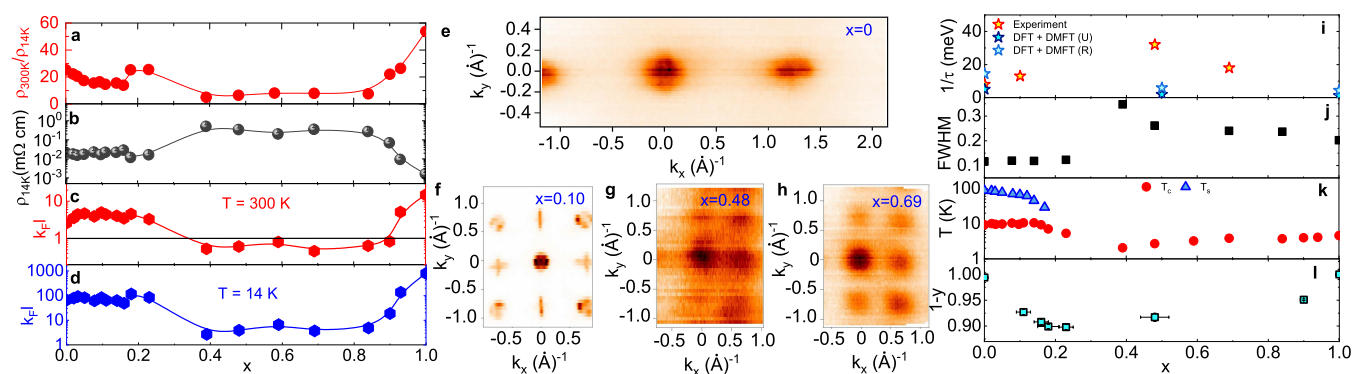

Figure 2. (a) Ratio of resistivity at 300 K to resistivity at 14 K and (b) resistivity values at 14 K. (c,d) Values of $k_F l$ for ($0 \leq x \leq 1$) at 300 K and at 14 K, respectively. Fermi surface near the Γ-point in the Brillouen zone for FeSe (e), $Fe_{1-y}Se_{0.9}S_{0.1}$ (f), $Fe_{1-y}Se_{0.52}S_{0.48}$ (g), and $Fe_{1-y}Se_{0.31}S_{0.69}$ (h). (i) Scattering rates at the Γ-point from experiment. Smearing of the Fermi surfaces in (e–h) gives an impression of the scattering rates, derived from the energy dispersion curves.[30] High $1/\tau$ is a hallmark of disorder-related electron scattering. Note how experimental $1/\tau$ is enhanced near $x = 0.5$, which is in contrast to the smooth evolution of the calculated $1/\tau$ due to the changes in the electronic correlations. (j) fwhm of single crystal diffraction [001] peaks in Figure 1k. Larger fwhm indicates higher disorder along the crystallographic c-axis Bragg planes. (k) $T_s(x)$ and $T_c(x)$. (l) Fe stoichiometry variation with respect to x.

Anderson localization for pointlike scatterers,[24] indicating the inadequacy of the Boltzmann transport model. Moreover, violation of Matthiessen's rule is inconsistent with the Mooij law, where increased disorder when electron–phonon scattering is present results in a decrease in temperature-dependent resistivity. Disorder and bad metal behavior are present in many unconventional superconductors.[25–27] Yet, experimental scattering rates $1/\tau$ in the bad metal state for $x \sim 0.5$ are much stronger than $1/\tau$ due to electronic correlations and in violation of Mooij's law. This implies that charge carriers might be inelastically scattered by spin fluctuations that are induced by nanoscale Fe–Ch bond disorder.[28] The present

study points to the need for future studies on the role of nanoscale iron-chalcogen bond distance inhomogeneity in electron correlation tuning as well as on the charge-nematic or magnetic spin fluctuations in highly disordered S-doped FeSe where superconducting T_c shows correlation with disorder-related scattering.[27–29]

Unit cell refinements of X-ray diffraction (XRD) powder patterns of $Fe_{1-y}Se_{1-x}S_x$ ($0 \leq x \leq 1$, $y \leq 0.1$) confirm phase purity.[30] Scanning transmission electron microscopy (STEM) images recorded by high-angle annular dark-field detector (HAADF) (Figure 1a–j) suggest the presence of nanoscale inhomogeneity and up to about 10% Fe vacancy defects that

develop for all crystals with mixed composition of Se and S on chalcogen atomic sites.[30] The contrast of Fe columns is stronger than that of S/Se columns in FeS, $Fe_{1-y}Se_{0.06}S_{0.94}$, and $Fe_{1-y}Se_{0.31}S_{0.69}$ but becomes weaker in $Fe_{1-y}Se_{0.82}S_{0.18}$ and FeSe. The peak intensity map shows the intensity variation of Fe and Se/S columns, indicating disordered Fe atomic vacancies. Single crystal X-ray diffraction (XRD) patterns (Figure 1k) shows (00l) reflections. The reflections shift to higher scattering angles with increasing x, consistent the decrease of the unit cell volume. The nematic transition T_s in FeSe, detected via the dip anomaly in $\rho(T)$, gradually shifts to $T_c \to 0$ as S substitutes for Se in the lattice and vanishes above $x = 0.18$ (Figure 1l,m); T_c increases weakly up to about 11 K for $x = 0.1$ (Figure 1n) which is in agreement with previous observations.[31−34] The width of the resistivity transition around T_c broadens as x increases from 0 and T_c reaches its minimum value of 2.1 K for all $0 \le x \le 1$ at $x = 0.4$ (Figure 1n,o). For higher S content approaching FeS, T_c increases (Figure 1o), consistent with T_c seen in $\chi(T)$.[30]

To estimate the disorder-related scattering, we consider $\rho(300\,K)/\rho(14\,K)$ as the residual resistivity ratio (RRR) for all x in (Figure 1l−o). In general, smaller values denote larger disorder-related scattering strength. There is a continuous decrease of RRR from $x = 0$ to $x = 0.16$ as S atoms substitute for Se and as the structural transition is suppressed (Figure 2a). When the structural/nematic transition is completely suppressed, the RRR increases to about 25. The RRR decreases with further increase in x up to $x = 0.4$ then shows a weak increase up to $x = 0.84$, and finally steeply rises to 54 at $x = 1$. The RRR changes with respect to x are also reflected in the residual resistivity values in the normal state close to T_c, ρ_{14K} (Figure 2b). Although ρ_{14K} involves contribution of different scattering mechanisms, higher values may signal larger contributions from the disorder component. Disorder contributes to dephasing of the electronic wave function in the normal state, although for weak disorder $k_Fl \gg 1$ the superconducting T_c in an isotropic s-wave superconductor should be unaffected by nonmagnetic impurities.[17,35,36] We estimate k_Fl in our samples as follows: in the Drude theory, the 2D resistivity is $\rho = (h/e^2)(d/k_Fl)$, where h is the Planck constant, e is the elementary charge, k_F is the Fermi wavenumber, d is interplane atomic distance, and l is mean free path. Approximating d by the value of the lattice parameter a at 300 K,[30] which changes less than 1% down to 10 K,[37] and using the experimental ρ values (Figure 2b),[30] we plot k_Fl versus x in Figure 2c (300 K) and Figure 2d (14 K). T_c (Figure 1n,o) is suppressed for strong disorder.

Strong disorder (Figure 2c,d) affects angle-resolved photoemission (ARPES) electronic scattering rates $1/\tau$. There is a considerable change in the Fermi surface near the Γ point (Figure 2e−h), as seen in $1/\tau$ when x is tuned from FeSe (Figure 2e) to a weakly disordered ($x = 0.1$) (Figure 2f) and then strongly disordered ($x = 0.48$ and 0.69) (Figure 2g,h) state toward FeS.[30,38] We plot experimental scattering rates and the scattering rates due to the change in electronic correlations calculated based on a combination of dynamical mean field theory (DMFT) and density functional theory (DFT) in Figure 2i for different x. Within the DFT + DMFT framework, larger scattering rates correspond to an increase in the electronic incoherence of states near the Fermi energy. This indicates that scattering rates due to solely local electronic correlations are reduced by increasing x in $Fe_{1-y}Se_{1-x}S_x$. However, the calculated scattering rates are very small when

compared to ARPES scattering rates at the Γ-point. The degree of correlations within the model is governed by Fe−Se and Fe−S bond distances, yet experimental scattering rate changes cannot be explained by the decrease of electronic correlations with x.

Whereas $1/\tau$ due to electronic correlations show an expected decrease as the content of sulfur atoms is increased in the lattice at the expense of Se,[39,30] observed $1/\tau$ are much larger, in particular near the middle of the alloy series. Larger ARPES scattering rates are found in samples with smaller RRR (Figure 2a). Increased scattering rates near the middle of the x range coincide with increased Bragg plane disorder along the c-axis (Figure 2j). Although $T_s(x)$ and $T_c(x)$ ($0 \le x \le 1$) (Figure 2k) match well with that previously observed,[40] we note that complete suppression of T_s coincides with reduction of the residual resistivity ratio (RRR) at $x = 0.18$ (Figure 2a), that is, with weak (Figure 2d) crystallographic disorder-related scattering.[41,42] T_c is suppressed only when disorder is strong ($k_Fl \sim 1$) just above T_c (Figure 2d) and when c-axis Bragg plane disorder is enhanced (Figure 2j). Although Fe vacancy defects are detected in all crystals by STEM-HAADF (Figure 1a−j), from synchrotron Rietveld refinement we conclude that defect content is negligible in the sample bulk for FeSe and FeS,[30] whereas Fe defect content increases up to about $x = 0.23$ (Figure 2l), coinciding with T_s suppression. Interestingly, increasing Fe vacancy defects in the nematic region does not significantly influence disorder effects on the electrical conductivity at low temperatures, as seen by the negligible changes in k_Fl (Figure 2d).

In metals, the scattering rate $1/\tau = (1/\tau_e + 1/\tau_i)$ is the sum of elastic $1/\tau_e$ and inelastic component $1/\tau_i$. Impurities and crystallographic defects/disorder commonly contribute to elastic scattering. However, bond lengths regulate the Fe−Ch overlap and the $FeCh_4$ tetrahedron shape which in turn controls the crystal field levels and thus the orbital occupancies and relative mixing of Fe d_{xz} and d_{yz} orbitals.[43,28] Se/S atom disorder may give rise to inelastic carrier scattering off charge-nematic or magnetic spin fluctuations that are enhanced due to variable Fe−Se and Fe−S hybridization.[28,43−46] Evidence for Se/S atom disorder in the tetrahedral surroundings of the Fe atoms comes from STEM-HAADF images (Figure 3a,b). From the refinements (Figure 3c), we obtain that the full width at half-maximum (fwhm) values are 0.15(3) nm (Fe peak) and 0.20(5) nm (Se/S peak) for $Fe_{1-y}Se_{0.31}S_{0.69}$, and 0.19(1) nm (Fe) and 0.10(5) nm (Se/S) for $Fe_{1-y}Se_{0.06}S_{0.94}$, respectively. Hence, chalcogen atomic positions are substantially more disordered near the middle range of S substitution on Se atomic sites.

Now we turn our attention to normal state scattering at high temperature for high disorder. The temperature dependence of $\rho(T)$ for $x \ge 0.4$ (Figure 1m) might hint at the phonon-related scattering. To clarify this, we focus on the Bloch-Grüneisen (BG) phonon scattering mechanism

$$\rho(T) = \rho_0 + A\left(\frac{T}{\theta_D}\right)^n \int_0^{\theta_D/T} \frac{z^5}{(e^z - 1)(1 - e^{-z})}\,dz$$

Using Debye temperatures θ_D obtained from heat capacity measurements on $Fe_{1-y}Se_{0.52}S_{0.48}$ and FeS,[30] we observe that the BG model provides an explanation for the resistivity at low temperatures but cannot explain the resistivity above about 150 K due to enhanced scattering above the phonon-related resistivity (Figure 4a,b). We plot the Mott resistivity ρ_{Mott} for
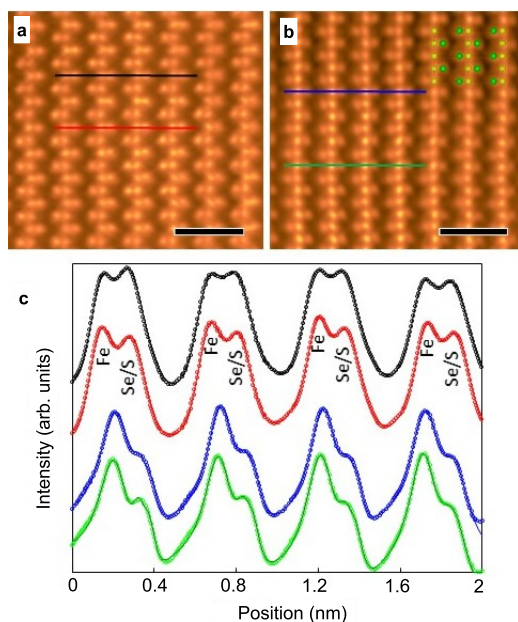
Figure 3. (a,b) STEM-HAADF images with the incident beam along the [100] direction for (a) $Fe_{1-y}Se_{0.31}S_{0.69}$ and (b) $Fe_{1-y}Se_{0.06}S_{0.94}$ single crystals. The [100] projection of the structure model is illustrated in (b) with yellow and green spheres representing Fe and Se/S atom, respectively. Scale bar 1 nm. (c) Intensity profiles (circles) from the scan lines shown in (a,b) with the corresponding colors. The solid lines are the fitted curves based on combined Gaussian and Lorentzian functions.

which $k_F l = 1$ and $\rho(T)/\rho_{Mott}$ for all x in Figure 4c,d. The $\rho(T)$ curves for $(0.39 \leq x \leq 0.9)$ (Figure 4d) retain metallic behavior $(d\rho/dT > 0)$ at high $T \sim 300$ K, even though $k_F l < 1$, that is, the scattering rate is beyond Mott limit, suggesting an exotic scattering mechanism.[47] Bad metal behavior with nearly linear-in-temperature resistivity is a hallmark of Hund's metals in the incoherent regime.[27,48−50]

In the small x regime, disorder can be screened by the strong correlations.[51] An increase in ρ_{300K}/ρ_{14K} when T_s is suppressed with x (Figure 2a,k) points to an interplay of increased disorder and sudden absence of nematic correlations, implying that strong correlations could be intertwined with strong disorder when there is significant sulfur substitution. The prefactor A in resistivity is related to the electron−phonon coupling constant and is generally not very large, since $\lambda \approx (0.1−0.3)$ in known materials. In normal metals for $T \gg \theta_D$ resistivity usually follows a $\rho = \rho_0 + AT$ linear temperature dependence which, extrapolated to very high temperatures, reaches the Mott limit far above melting temperature. When disorder is added, this increases ρ_0, but when electron−phonon scattering is present A generally decreases with adding disorder and could even change sign at strong disorder where ρ_0 is of the order of the Mott limit; this well documented behavior is known as the Mooij correlation.[52] The electron−phonon scattering can push the resistivity up to the Mott limit only if the disorder is already strong so that ρ_0 is near the Mott limit itself, but then the temperature-dependent resistivity term is commonly smaller when compared to the case without disorder.

Our observations are inconsistent with the Mooij scenario. First, we note the temperature-dependent part (Figure 4a,b) - i.e. the slope A of Bloch-Grüneisen resistivity fits - is much smaller for FeS when compared to $Fe_{1-y}Se_{0.52}S_{0.48}$,[30] contrary

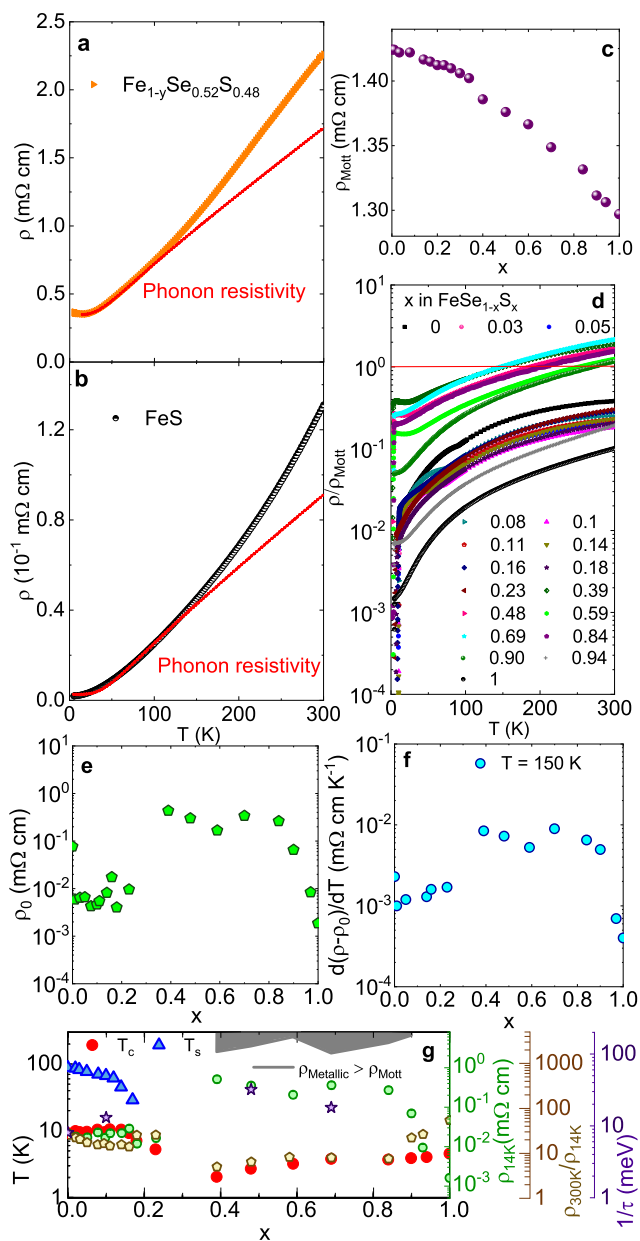**Figure 4.** Data and Bloch-Grüneisen phonon scattering simulation are depicted in (a,b) using $\theta_D = 240(5)$ K for FeS and $\theta_D = 208(1)$ K for $FeSe_{0.52}S_{0.48}$ obtained from low-temperature heat capacity fits, respectively (see text). Mott limit resistivity $\rho_{Mott}(x)$ at 300 K (c), and $\rho(T)/\rho_{Mott}$ for all x in $Fe_{1-y}Se_{1-x}S_x$ (d). Red line in (d) denotes Mott limit $k_F l = 1$. (e) Residual resistivity $\rho(T \rightarrow 0) = \rho_0$. (f) Resistivity slope at 150 K. (f) Summary of experimental scattering and transport properties at $Fe_{1-y}Se_{1-x}S_x$ ($0 \leq x \leq 1$, $y \leq 0.1$) phase diagram.

to Mooij scenario.[52] Next, let us have a look at $\rho(T)$ as x is reduced. For $x = 0.93$ and $x = 1$, ρ_0 is very small, and yet the high-temperature slope of $\rho(T)$ is much smaller when compared to x near the middle range of S atom substitution (Figure 4e,f), so that resistivity does not reach Mott limit at 300 K. As x is reduced from 1 in $Fe_{1-y}Se_{1-x}S_x$, ρ_{14K} increases more than 1 order of magnitude when compared to ρ_{14K} for FeS (Figure 2b) while temperature-dependent part of $\rho(T)$ also increases. This is unrelated to a reduction in the carrier density n. In contrast, n is increased as x is reduced from 1.[30] For example, already for $x = 0.9$ the slope is much larger when

compared to $x = 0.93$, and as seen in the slope of $\rho(T)$, this trend continues toward the middle of the alloy series (Figure 4f).[30,52] This is in contrast to the Mooij relation where the interplay of phonon scattering and disorder induces a slope decrease at stronger disorder. In Matthiessen's rule, $\rho(T) = \rho_0 + \rho_1(T)$, ρ_0 is attributed to disorder, whereas the temperature-dependent part $\rho_1(T)$ is related to various inelastic channels or correlations which are assumed independent of disorder. Increasing disorder should give an increase of ρ_0 but should not modify the slope of $\rho_1(T)$ for weak disorder, whereas for strong disorder the slope decreases and eventually changes sign.[52] This should give a simple upward shift of the entire $\rho(T)$ curve on a linear scale, not on a logarithmic scale. Resistivity data for strong disorder indicate violation of Matthiessen's rule, contrary to Mooij's law. The fact that the $x = 0.9$ and $x = 0.94$ curves shift on a logarithmic scale indicates that increasing residual resistivity also increases temperature-dependent resistivity.

In Figure 4g, we present a summary of all transport and scattering properties. For the region of x where metallic resistivity exceeds the Mott limit at high temperature, disorder is strong (Figure 2c,d) and superconducting T_c is suppressed. The evolution of $T_c(x)$ follows the evolution of disorder-related scattering (RRR) with x, whereas it shows inverse trend with residual resistivity just above T_c (ρ_{14K}) and ARPES scattering rate at the Γ-point in the Brillouen zone $1/\tau$. This points to an order parameter with nodes that gets averaged over the Fermi surface and thus reduced by scattering along with the T_c.

In summary, nanoscale inhomogeneity in $Fe_{1-y}Se_{1-x}S_x$ ($0 \leq x \leq 1$, $y \leq 0.1$) results in Fe atomic vacancies and Fe–S and Fe–Se bond disorder. As x is increased and material evolves away from FeSe, there is a rise in Fe atomic vacancies and T_s is suppressed for weak disorder. Superconducting T_c in the regime of strong disorder develops on cooling from a high-temperature metallic normal state resistivity that exceeds Mott limit and violates Matthiessen's rule and the Mooij law, implying that the scattering mechanism is unrelated to phonons. This behavior is in contrast to a disorder driven metal–insulator transition[17] where $d\rho/dT < 0$. When impurities are added to the relatively good metals FeSe and FeS, the additional scattering depends on doping in a manner that is inconsistent with the standard picture of weak disorder. We expect that our findings will stimulate further experiments and theoretical methods to connect nanoscale inhomogeneity with scattering mechanism and it is conceivable that broader distribution of Fe-chalcogen bond lengths activates charge-nematic or magnetic spin fluctuations that are the dominant source of scattering for the intermediate values of x.

■ ASSOCIATED CONTENT

ⓢ Supporting Information

The Supporting Information is available free of charge at https://pubs.acs.org/doi/10.1021/acs.nanolett.2c01282.

> Materials synthesis and experimental methods, crystal structure, magnetic susceptibility, Bloch-Grüneisen model for $\rho(T)$ for high x, ARPES scattering rates, DFT + DMFT scattering rates, resistivity slope and carrier concentration (PDF)

■ AUTHOR INFORMATION

Corresponding Authors

Aifeng Wang — *Condensed Matter Physics and Materials Science Department, Brookhaven National Laboratory, Upton, New York 11973, United States;* Present Address: College of Physics, Chongqing University, Chongqing 401331, China; ⓞ orcid.org/0000-0003-2425-3259; Email: aafwang@cqu.edu.cn

Cedomir Petrovic — *Condensed Matter Physics and Materials Science Department, Brookhaven National Laboratory, Upton, New York 11973, United States; Department of Materials Science and Chemical Engineering, Stony Brook University, Stony Brook, New York 11790, United States;* ⓞ orcid.org/0000-0001-6063-1881; Email: petrovic@bnl.gov

Authors

Lijun Wu — *Condensed Matter Physics and Materials Science Department, Brookhaven National Laboratory, Upton, New York 11973, United States*

Qianheng Du — *Condensed Matter Physics and Materials Science Department, Brookhaven National Laboratory, Upton, New York 11973, United States; Department of Materials Science and Chemical Engineering, Stony Brook University, Stony Brook, New York 11790, United States; Present Address: Materials Science Division, Argonne National Laboratory, Lemont, Illinois 60439, U.S.A.*

Muntaser Naamneh — *Department of Physics, Ben-Gurion University of the Negev, Beer-Sheva 84105, Israel*

Walber Hugo Brito — *Departamento de Física, Universidade Federal de Minas Gerais, 30123-970 Belo Horizonte, Minas Gerais, Brazil*

AM Milinda Abeykoon — *National Synchrotron Light Source II, Brookhaven National Laboratory, Upton, New York 11973, United States*

Wojciech Radoslaw Pudelko — *Swiss Light Source, Paul Scherrer Institut, CH-5232 Villigen, Switzerland; Physik-Institut, Universität Zürich, CH-8057 Zürich, Switzerland*

Jasmin Jandke — *Swiss Light Source, Paul Scherrer Institut, CH-5232 Villigen, Switzerland*

Yu Liu — *Condensed Matter Physics and Materials Science Department, Brookhaven National Laboratory, Upton, New York 11973, United States; Present Address: Los Alamos National Laboratory, Los Alamos, New Mexico 87545, U.S.A.;* ⓞ orcid.org/0000-0001-8886-2876

Nicholas C. Plumb — *Swiss Light Source, Paul Scherrer Institut, CH-5232 Villigen, Switzerland*

Gabriel Kotliar — *Condensed Matter Physics and Materials Science Department, Brookhaven National Laboratory, Upton, New York 11973, United States; Department of Physics and Astronomy, Center for Materials Theory, Rutgers University, Piscataway, New Jersey 08854, United States*

Vladimir Dobrosavljevic — *Department of Physics and National High Magnetic Field Laboratory, Florida State University, Tallahassee, Florida 32306, United States*

Milan Radovic — *Swiss Light Source, Paul Scherrer Institut, CH-5232 Villigen, Switzerland*

Yimei Zhu — *Condensed Matter Physics and Materials Science Department, Brookhaven National Laboratory, Upton, New York 11973, United States;* ⓞ orcid.org/0000-0002-1638-7217

Complete contact information is available at:
https://pubs.acs.org/10.1021/acs.nanolett.2c01282

◼ REFERENCES

(1) Liang, Q.; Zhang, Q.; Zhao, Q.; Liu, M.; Wee, A. T. S. Defect Engineering of Two-Dimensional Transition-Metal Dichalcogenides: Applications, Challenges, and Opportunities. *ACS Nano* **2021**, *15*, 2165−2181.

(2) Ryder, C. R.; Wood, J. D.; Wells, S. A.; Hersam, M. C. Chemically Tailoring Semiconducting Two-Dimensional Transition Metal Dichalcogenides and Black Phosphorus. *ACS Nano* **2016**, *10*, 3900−3917.

(3) Zhong, J.; Stocks, G. M. Localization/Quasi-Delocalization Transitions and Quasi-Mobility-Edges in Shell-Doped Nanowires. *Nano Lett.* **2006**, *6*, 128−132.

(4) Utterback, J. K.; Sood, A.; Cropceanu, I.; Guzelturk, B.; Talapin, D. V.; Lindenberg, A. M.; Ginsberg, N. S. Nanoscale Disorder Generates Subdiffusive Heat Transport in Self-Assembled Nanocrystal Films. *Nano Lett.* **2021**, *21*, 3540−3547.

(5) Boltzmann, L. *Lectures on Gas Theory*; University of California Press: Los Angeles, 1964.

(6) Cercignani, C. *The Boltzmann Equation and Its Applications*; Springer: New York, 1988.

(7) Mertig, I. Transport properties of dillute alloys. *Rep. Prog. Phys.* **1999**, *62*, 237−276.

(8) Aronov, A. G.; Gal'perin, Yu. M.; Gurevich, V. L.; Kozub, V. I. Weighted Monte Carlo approach to electron transport in semiconductors. *Adv. Phys.* **1981**, *30*, 539−592.

(9) Rossi, F.; Poli, P.; Jacobini, C. The Boltzmann-equation description of transport in superconductors. *Semicond. Sci. Technol.* **1992**, *7*, 1017−1035.

(10) Walker, D. J. C.; Mackenzie, A. P.; Cooper, J. R. Transport properties of zinc-doped $YBa_2Cu_3O_{7-\delta}$ thin films. *Phys. Rev. B* **1995**, *51*, 15653−15656.

(11) Prozorov, R.; Konczykowski, M.; Tanatar, M. A.; Wen, H.-H.; Fernandes, R. M.; Canfield, P. C. Interplay between superconductivity and itinerant magnetism in underdoped $Ba_{1-x}K_xFe_2As_2$ (x = 0.2) probed by the response to controlled point-like disorder. *npj Quantum Materials* **2019**, *4*, 34.

(12) Wang, Y.; Bosse, G.; Nair, H. P.; Schreiber, N. J.; Ruf, J. P.; Cheng, B.; Adamo, C.; Shai, D. E.; Lubashevsky, Y.; Schlom, D. G.; Shen, K. M.; Armitage, N. P. Subterahertz Momentum Drag and Violation of Matthiesen's Rule in an Ultraclean Ferromagnetic $SrRuO_3$ Metallic Thin Films. *Phys. Rev. Lett.* **2020**, *125*, 217401.

(13) Fisk, Z.; Webb, G. W. Saturation of the high-temperture normal-state electrical resistivity of superconductors. *Phys. Rev. Lett.* **1976**, *36*, 1084−1086.

(14) Gunnarsson, O.; Calandra, M.; Han, J. E. Colloquium: saturation of electrical resistivity. *Rev. Mod. Phys.* **2003**, *75*, 1085−1099.

(15) Anderson, P. W. Absence of diffusion in certain random lattices. *Phys. Rev.* **1958**, *109*, 1492−1505.

(16) Mooij, J. H. Electrical conduction in concentrated disordered transition metal alloys. *J. Phys. Status Solidi* **1973**, *17*, 521.

(17) Lee, P. A.; Ramakrishnan, T. V. Disordered electronic systems. *Rev. Mod. Phys.* **1985**, *57*, 287.

(18) Hsu, F.-C.; Luo, J.-Y.; Yeh, K.-W.; Chen, T.-K.; Huang, T.-W.; Wu, P. M.; Lee, Y.-C.; Huang, Y.-L.; Chu, Y.-Y.; Yan, D.-C.; Wu, M.-K. Superconductivity in the PbO-type structure α-FeSe. *Proc. Natl. Acad. Sci. U.S.A.* **2008**, *105*, 14262−14264.

(19) Lai, X.; Zhang, H.; Wang, Y.; Wang, X.; Zhang, X.; Lin, J.; Huang, F. Observation of Superconductivity in Tetragonal FeS. *J. Am. Chem. Soc.* **2015**, *137*, 10148−10151.

(20) Chowdhury, D.; Berg, E.; Sachdev, S. Nematic order in the vicinity of a vortex in superconducting FeSe. *Phys. Rev. B* **2011**, *84*, 205113.

(21) Baek, S-H.; Efremov, D. V.; Ok, J. M.; Kim, J. S.; van den Brink, J.; Buchner, B. Orbital-driven nematicity in FeSe. *Nat. Mater.* **2015**, *14*, 210−214.

(22) Massat, P.; Farina, D.; Paul, I.; Karlsson, S.; Strobel, P.; Toulemonde, P.; Measson, M.-A.; Cazayous, M.; Sacuto, A.; Kasahara, S.; Shibauchi, T.; Matsuda, Y.; Gallais, Y. Charge-induced nematicity in FeSe. *Proc. Natl. Acad. Sci. U.S.A.* **2016**, *113*, 9177−9181.

(23) Wang, F.; Kivelson, S. A.; Lee, D.-H. Nematicity and quantum paramagnetism in FeSe. *Nat. Phys.* **2015**, *11*, 959−963.

(24) Lagendijk, A.; van Tiggelen, B.; Wiersma, D. S. Fifty years of Anderson localization. *Phys. Today* **2009**, *62*, 24−29.

(25) Emery, V. J.; Kivelson, S. A. Superconductivity in bad metals. *Phys. Rev. Lett.* **1995**, *74*, 3253.

(26) Haule, K.; Shim, J. H.; Kotliar, G. Correlated electronic structure of $LaO_{1-x}F_xFeAs$. *Phys. Rev. Lett.* **2008**, *100*, 226402.

(27) Haule, K.; Kotliar, G. Coherence−incoherence crossover in the normal state of iron oxypnictides and importance of Hunds rule coupling. *New. J. Phys.* **2009**, *11*, 025021.

(28) Yin, Z. P.; Haule, K.; Kotliar, G. Kinetic frustration and the nature of the magnetic and paramagnetic states in iron pnictides and iron chalcogenides. *Nat. Mater.* **2011**, *10*, 932.

(29) Taillefer, L. Scattering and Pairing in Cuprate Superconductors. *Annu.Rev.Condens.Matter Phys.* **2010**, *1*, 51−70.

(30) See Supporting Information.

(31) Hosoi, S.; Matsuura, K.; Ishida, K.; Wang, H.; Mizukami, Y.; Watashige, T.; Kasahara, S.; Matsuda, Y.; Shibauchi, T. Nematic quantum critical point without magnetism in $FeSe_{1-x}S_x$ superconductors. *Proc. Natl. Acad. Sci. U. S. A.* **2016**, *113*, 8139.

(32) Mizuguchi, Y.; Tomioka, F.; Tsuda, S.; Yamaguchi, T.; Takano, Y. Substitution Effects on FeSe Superconductor. *J. Phys. Soc. Jpn.* **2009**, *78*, 074712.

(33) Liu, Y.; Wang, A.; Ivanovski, V. N.; Du, Q.; Koteski, V.; Petrovic, C. Thermoelectricity and electronic correlation enhancement in FeS by light Se doping. *Phys. Rev. B* **2022**, *105*, 045133.

(34) Wang, A.; Milosavljevic, A.; Abeykoon, A. M. M.; Ivanovski, V.; Du, Q.; Baum, A.; Stavitski, E.; Liu, Y.; Lazarevic, N.; Attenkofer, K.; Hackl, R.; Popovic, Z.; Petrovic, C. Suppression of Superconductivity and Nematic Order in $Fe_{1-y}Se_{1-x}S_x$ ($0 \leq x \leq 1$; $y \leq 0.1$) Crystals by Anion Height Disorder. *Inorg. Chem.* **2022**, *61*, 11036−11045.

(35) Anderson, P. Absence of Diffusion in Certain Random Lattices. *Phys. Rev.* **1958**, *109*, 1492−1505.

(36) Anderson, P. Theory of dirty superconductors. *J. Phys. Chem. Solids* **1959**, *11*, 26−30.

(37) Margadonna, S.; Takabayashi, Y.; McDonald, M. T.; Kasperkiewicz, K.; Mizuguchi, Y.; Takano, Y.; Fitch, A. N.; Suard, E.; Prassides, K. Crystal structure of the new $FeSe_{1-x}$ superconductor. *Chem. Commun.* **2008**, *43*, 5607.

(38) Hoesch, M.; Gannon, L.; Shimada, K.; Parrett, B. J.; Watson, M. D.; Kim, T. K.; Zhu, X.; Petrovic, C. Disorder Quenching of the Charge Density Wave in $ZrTe_3$. *Phys. Rev. Lett.* **2019**, *122*, 017601.

(39) Coldea, A. I.; Blake, S. F.; Kasahara, S.; Haghighirad, A. A.; Watson, M. D.; Knafo, W.; Choi, E. S.; McCollam, A.; Reiss, P.; Yamashita, T.; Bruma, T.; Speller, S. C.; Matsuda, Y.; Wolf, T.; Shibauchi, T.; Schofield, A. J. Evolution of the low-temperature Fermi surface of superconducting $FeSe_{1-x}S_x$ across a nematic phase transition. *NPJ. Quant. Mater.* **2018**, *4*, eaar6419.

(40) Yi, X.; Xing, X.; Qin, L.; Feng, J.; Li, M.; Zhang, Y.; Meng, Y.; Zhou, N.; Sun, Y.; Shi, Z. Hydrothermal synthesis and complete phase diagram of $FeSe_{1-x}S_x$ $(0 \leq x \leq 1)$ single crystals. *Phys. Rev. B* **2021**, *103*, 144501.

(41) Böhmer, A. E.; Taufour, V.; Straszheim, W. E.; Wolf, T.; Canfield, P. C. Variation of transition temperatures and residual resistivity ratio in vapor-grown FeSe. *Phys. Rev. B* **2016**, *94*, 024526.

(42) Rössler, S.; Huang, C. L.; Jiao, L.; Koz, C.; Schwarz, U.; Wirth, S. Influence of disorder on the signature of the pseudogap and multigap superconducting behavior in FeSe. *Phys. Rev. B* **2018**, *97*, 094503.

(43) Fernandes, R. M.; Chubukov, A. V.; Schmalian, J. What drives nematic order in iron-based superconductors. *Nat. Phys.* **2014**, *10*, 97.

(44) Rømer, A. T.; Hirschfeld, P. J.; Andersen, B. M. Raising the Critical Temperature by Disorder in Unconventional Superconductors Mediated by Spin Fluctuations. *Phys. Rev. Lett.* **2018**, *121*, 027002.

(45) Glamazda, A.; Lemmens, P.; Ok, J. M.; Kim, J. S.; Choi, K. Y. Dichotomic nature of spin and electronic fluctuations in FeSe. *Phys. Rev. B* **2019**, *99*, 075142.

(46) Ruiz, H.; Wang, Y.; Moritz, B.; Baum, A.; Hackl, R.; Devereaux, T. P. Frustrated magnetism from local moments in FeSe. *Phys. Rev. B* **2019**, *99*, 125130.

(47) Takagi, H.; Batlogg, B.; Kao, H. L.; Kwo, J.; Cava, R. J.; Krajewski, J. J.; Peck, W. F., Jr. Systematic Evolution of Temperature-Dependent Resistivity in $La_{2-x}Sr_xCuO_4$. *Phys. Rev. Lett.* **1992**, *69*, 2975−2972.

(48) Allen, P. B.; Berger, H.; Chauvet, O.; Forro, L.; Jarlborg, T.; Junod, A.; Revaz, B.; Santi, G. Transport properties, thermodynamic properties and electronic structure of $SrRuo_3$. *Phys. Rev. B* **1996**, *53*, 4393.

(49) Dang, H. T.; Mravlje, J.; Georges, A.; Millis, A. J. Electronic correlations, magnetism, and Hund's rule coupling in the ruthenium perovskites $SrRuO_3$ and $CaRuO_3$. *Phys. Rev. B* **2015**, *91*, 195149.

(50) Deng, X.; Haule, K.; Kotliar, G. Transport Properties of Metallic Ruthenates, a DFT+DMFT Investigation. *Phys. Rev. Lett.* **2016**, *116*, 256401.

(51) Tanaskovic, D.; Dobrosavljevic, V.; Abrahams, E.; Kotliar, G. Disorder Screening in Strongly Correlated Systems. *Phys. Rev. Lett.* **2003**, *91*, 066603.

(52) Ciuchi, S.; Di Sante, D.; Dobrosavljevic, V.; Fratini, S. The origin of Mooij correlations in disordered metals. *NPJ. Quantum Materials* **2018**, *44*, 3.

📖 **Recommended by ACS**

Dynamic Observation of Topological Soliton States in a Programmable Nanomechanical Lattice

Shaochun Lin, Jiangfeng Du, *et al.*

JANUARY 13, 2021
NANO LETTERS   READ 🗗

Two-Dimensional Magnets beyond the Monolayer Limit

Andrey M. Tokmachev, Vyacheslav G. Storchak, *et al.*

JUNE 15, 2021
ACS NANO   READ 🗗

Third-Order Optical Nonlinearity of Three-Dimensional Massless Dirac Fermions

J. L. Cheng, S. W. Wu, *et al.*

JULY 27, 2020
ACS PHOTONICS   READ 🗗

Néel Vector Induced Manipulation of Valence States in the Collinear Antiferromagnet Mn_2Au

H. J. Elmers, M. Jourdan, *et al.*

NOVEMBER 25, 2020
ACS NANO   READ 🗗

Get More Suggestions >